Research Article | Open Access

Microstructures

Yao et al. Microstructures 2026, 6, 2026087 DOI:10.20517/microstructures.2026.06

Emerging medium-range order in deformed Zr-based bulk metallic glasses during sub-T_g relaxation

Zhongzheng Yao[1,#], Sinan Liu[1,3,#], Jiacheng Ge[1,3], Huiqiang Ying[1], Wentao Zhang[1], Yao Jiang[1], Huaijun Lin[4], Kaveh Edalati[5], He Zhu[1,2], Zhenduo Wu[6], Jianrong Zeng[7], Yang Ren[3], Xun-Li Wang[3], Si Lan[1,2,8]

Keywords:
Bulk metallic glass, shear bands, local structure, relaxation

Citation: Yao, Z.; Liu, S.; Ge, J.; Ying, H.; Zhang, W.; Jiang, Y.; Lin, H.; Edalati, K.; Zhu, H.; Wu, Z.; Zeng, J.; Ren, Y.; Wang, X. L.; Lan, S. Emerging medium-range order in deformed Zr-based bulk metallic glasses during sub-T_g relaxation. *Microstructures* **2026**, *6*, 2026087. https://dx.doi.org/10.20517/microstructures.2026.06

Received: 7 Jan 2026
First Decision: 23 Mar 2026
Revised: 3 Apr 2026
Accepted: 21 May 2026
Published: 24 Jun 2026

Academic Editor:
Xiaozhou Liao
Copy Editor:
Fangling Lan
Production Editor:
Fangling Lan

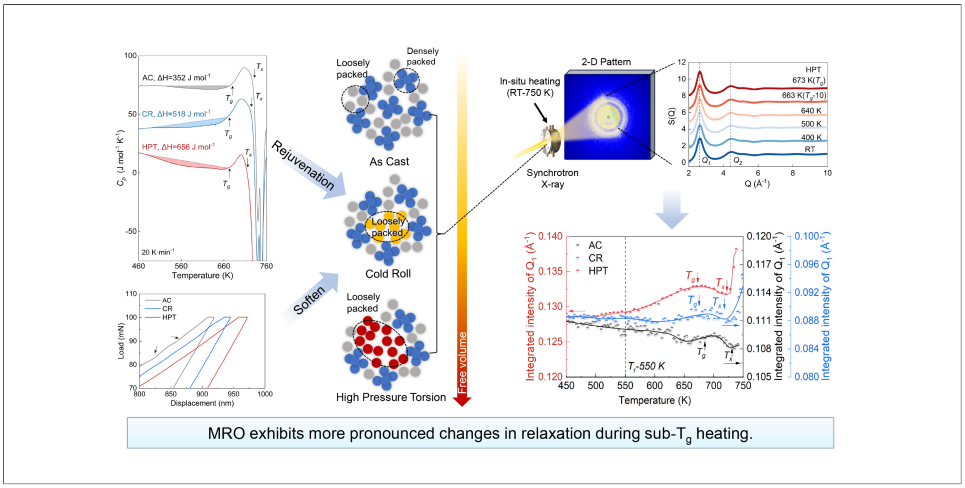

Abstract

The plasticity of bulk metallic glasses (BMGs) is closely correlated with the nature of shear bands; however, the structural origin of shear bands remains elusive due to the difficulty of obtaining direct observations. In this study, we investigated the microstructural evolution of shear bands during thermal relaxation by examining the local atomic-scale response to heating. $Zr_{52.5}Cu_{17.9}Ni_{14.6}Al_{10}Ti_5$ BMGs were subjected to two specifically designed deformation methods, namely, cold rolling and high-pressure torsion (HPT), to generate shear bands with varying volume fractions and rejuvenation states. *In situ* synchrotron diffraction results revealed a more pronounced growth of medium-range ordering at sub-T_g temperatures in the deformed BMGs than in the as-cast sample. The HPT-deformed BMG, with the highest volume fraction and distribution complexity of shear bands, demonstrated the most rapid increase in the ordering process. The transition of cluster connection modes

[1]School of Materials Science and Engineering/Herbert Gleiter Institute of Nanoscience, Nanjing University of Science and Technology, Nanjing 210094, Jiangsu, China.
[2]Key Laboratory of Advanced Nano Structures and Functional Materials Jiangsu Province Universities, Nanjing University of Science and Technology, Nanjing 210094, Jiangsu, China.
[3]Physics Department, City University of Hong Kong, Hong Kong SAR, China.
[4]Institute of Advanced Wear & Corrosion Resistance and Functional Materials, Jinan University, Guangzhou 510632, Guangdong, China.
[5]International Institute for Carbon-Neutral Energy Research (WPI-I2CNER), Kyushu University, Fukuoka 819-0395, Japan.
[6]Department of Materials Science and Engineering, City University of Hong Kong, Dongguan 523808, Guangdong, China.
[7]Shanghai Synchrotron Radiation Facility, Shanghai Advanced Research Institute, Chinese Academy of Sciences, Shanghai 201204, China.
[8]State Key Laboratory of Light Superalloys/Advanced Casting Technologies, Nanjing Belight Laboratory, Nanjing University of Science and Technology, Nanjing 210094, Jiangsu, China.
[#]Co-first author.

Correspondence to: Prof. He Zhu, School of Materials Science and Engineering/Herbert Gleiter Institute of Nanoscience, Nanjing

University of Science and Technology, Nanjing 210094, China. E-mail: hezhu@njust.edu.cn; Prof. Zhenduo Wu, Department of Materials Science and Engineering, City University of Hong Kong, Dongguan 523808, Guangdong, China. E-mail: zd.wu@cityu-dg.edu.cn; Prof. Si Lan, School of Materials Science and Engineering/Herbert Gleiter Institute of Nanoscience, Nanjing University of Science and Technology, Nanjing 210094, Jiangsu, China. E-mail: lansi@njust.edu.cn

possibly explained the anomalous emergence of medium-range order in the shear bands of deformed BMGs during sub-T_g relaxation or tension. Our study offers new insights into the atomic structure origins of shear bands, contributing to a deeper understanding of BMG plasticity.

INTRODUCTION

Bulk metallic glasses (BMGs) are characterized by a lack of long-range atomic order, but with unique short-range and medium-range order (SRO and MRO), endowing them with unique mechanical properties[1-5], such as high yield strength but limited ductility[6,7]. Inhomogeneous plastic deformation in BMGs under high stress or high strain rates[8,9] can induce a highly localized softening area along with the formation of shear bands (SBs)[10-12], leading to catastrophic fracture under uniaxial loading[13,14]. Various models have been proposed to determine microstructural evolution during plastic deformation in BMGs. The free volume theory postulates that macroscopic shear deformation can be attributed to the coordinated transition of multiple atoms into adjacent voids[8,15,16]. Alternatively, the shear transformation zone (STZ) model describes the plastic deformation of BMGs as a collective process involving numerous localized shear events within atomic clusters of varying configurations[17-19]. Other models, including those based on flow units[20,21], also suggest the presence of[22,23] microscopic regions with higher energy and atomic mobility than the surrounding matrix, similar to crystal defects. However, due to the extremely short timescales within highly localized regions, direct atomic-scale observations using conventional characterization techniques remain challenging. Therefore, obtaining a clear picture of the atomic structure of shear bands remains elusive.

It has been reported that increased free volume can enhance atomic diffusion and produce loosely packed structures with multiple softened regions[24]. Numerous experiments confirmed that this increase in free volume can lead to reduced hardness and elastic modulus, though with improved ductility[25-27]. Work softening of BMGs has also been associated with the accumulating of excess free volume in SBs[28-30]. Structure relaxation is known to induce the annihilation of excess free volume, resulting in structural homogenization and transition to a lower energy state. This process decreases soft regions and overall deformability[31,32]. The reverse process, known as rejuvenation, is described as a transition to a higher energy state[33-35]. Thermal cycling has been adopted as a non-destructive pathway to rejuvenate BMGs, as demonstrated by increased enthalpy and improved plasticity. Destructive methods, involving plastic deformation, such as cold rolling (CR)[36-38], high-pressure torsion (HPT)[39-41], and the confinement method[42-44], have been applied to improve the plasticity of glassy alloys. In plastic deformation methods, SBs with structural and dynamic inhomogeneities are introduced into the glasses[45]. Subsequently, the rejuvenation effect of plastic deformation has been confirmed by the increased exothermal enthalpy of the deformed MGs when heated to sub-T_g [46-48]. This plastic deformation has been shown to induce substantial stress concentrations and multiple shear transformations within the glassy matrix, resulting in a high density of confined shear bands and increased free volume. This controlled modification of structural inhomogeneities and free volume can facilitate the observation and analysis of atomic-scale dynamics and changes associated with shear bands. As a result, by examining the evolution of short-to-medium range order during relaxation, we can effectively elucidate the structural characteristics of shear bands within deformed BMGs.

This work introduced high-density SBs in the deformed Zr-based BMG via CR and HPT, as confirmed by differential scanning calorimetry and microscopy techniques. Nanoindentation and microcolumn compression tests were conducted to investigate the softening behavior of the samples in different rejuvenated states. Subsequent *in-situ* synchrotron high-energy X-ray diffraction revealed that, at sub-T_g temperatures, different deviations occurred from the linear relevance at the first moment of the first sharp diffraction peak (FSDP) among MGs with different deformation modes. Pair distribution function analysis indicated that the enhancement of structural ordering was due to the transition of cluster connection modes on MRO. Our results showed that the transformation of cluster connection modes may explain the anomalous growth of MRO in the shear bands of the deformed BMGs.

MATERIALS AND METHODS

Sample preparation

$Zr_{52.5}Cu_{17.9}Ni_{14.6}Al_{10}Ti_5$ BMG (i.e., BAM 11) plates with dimensions of 10 mm in width, 30 mm in length, and 1 mm in thickness, were prepared by arc melting, followed by copper-mold suction casting (Sky Technology Development Co., Ltd., China) under a Ti-gettered high-purity argon (Ar) atmosphere. Plates 10 mm in width and 1 mm in thickness were rolled on a rolling mill (Changzhou Xiechuang Mechanical Technology Co., Ltd., China). During the rolling process, the down-rolling amount was increased by 0.02 mm each time until the thickness of the plates reached 0.3 mm. Disks 1 mm in thickness and 10 mm in diameter were produced from the original BMG plate by electrical discharge machining (Taizhou Jinggong Electromechanical Manufacturing Co. Ltd., China). The BAM 11 disk, 10 mm in diameter and with a thickness of 1 mm, was placed between the HPT anvils (Japan), which had a diameter of 10 mm and contained a 0.3-mm-deep groove. During the HPT process, the discs were deformed for 10 revolutions at a rotation rate of 1 rpm under an applied pressure of 6 GPa at room temperature. To avoid possible errors induced by introducing different fractions of SBs, the HPT specimens used in the thermal and mechanical tests were obtained from the region of uniform shear deformation, ensuring uniform and severe plastic deformation[48].

Characterization of SBs

Specific heat capacity (C_p) experiments were carried out by differential scanning calorimetry (Mettler-Toledo, DSC-1, Switzerland) in a high-purity N_2 atmosphere at a flow rate of 50 mL·min^{-1}. The temperature range of the experiment was set to 323-773 K at a heating rate of 20 K min^{-1}. A sapphire sample was used as a reference for C_p measurement. An FEI Quanta 250 FEG (Oregon, USA) scanning electron microscope (SEM) was used to observe the SBs on the surfaces of the CR and HPT samples and the morphology of the nanoindentation area. High-resolution transmission electron microscopy measurements were performed via transmission electron microscopy (TEM, JEM-2100F, Japan).

Mechanical testing

The nanoindentation tests were carried out using an Agilent Nano Indenter G200 (California, USA) at room temperature with a typical Berkovich diamond indenter. The load was set from 0 to 100 mN at a loading rate of 5 mN s^{-1}, and the load was held at 100 mN for 10 s and then unloaded at the same rate as the loading process. Subsequently, eight points were measured for each sample to obtain the mean values. Micropillars with nominal diameters of ~2.5 μm and a height of around 5 μm were prepared by a focused ion beam (FIB) system (Zeiss Auriga, Germany) operated at an accelerating voltage of 30 keV using a Ga^+ focused ion beam. A two-step milling method was then employed with milling currents of 0.79 nA for coarse milling and 40 pA for fine polishing. Two specimens were prepared on the same individual sample, with a distance of more than 100 μm between them to avoid stress interactions. An FT-NMT03 nanomechanical *in situ* testing system (China) was used in the experiments, capable of performing *in situ* micropillar compression tests in a Zeiss Auriga FIB/SEM dual beam system. The experiments utilized a conical flat indenter made of diamond,

featuring a 10-μm flat tip at its apex, and indentation was performed at a constant loading rate of 10^{-3} s^{-1}.

High-energy X-ray synchrotron diffraction

High-energy X-ray synchrotron diffraction experiments were performed at the beamline 11-ID-C of the Advanced Photon Source (APS), Argonne National Laboratory (ANL, Illinois, USA). AC-BMG with a thickness of ~1 mm, CR- and HPT-BMG with a thickness of ~0.3 mm were mounted in a Linkam THMS600 furnace (United Kingdom) for thermal scanning. Then, high-energy X-rays with a beam size of 500 μm × 500 μm and wavelength of 0.01173 nm were used to perform transmission geometry for data collection. Measurements were conducted in a high-purity argon atmosphere. Two-dimensional (2D) diffraction patterns were obtained using a Perkin Elmer amorphous silicon detector with a data acquisition time of 1 s for each pattern. The time for data readout and storage was approximately 5 s, with a heating rate of 20 K min^{-1}. The time resolution was about 6 s, and the temperature resolution was 1-2 K. The static structure factor, $S(Q)$, was derived from the two- dimensional diffraction ring patterns by masking bad pixels, integrating images, subtracting the appropriate background, and correcting for oblique incidence, absorption, multiple scattering, fluorescence, Compton scattering, and Laue correction using Fit2D and PDFgetX2[49]. The reduced pair-distribution function (PDF) $G(r)$ profiles were obtained via the Fourier transform of $Q(S(Q)^{-1})$.

To analyze Q_1, the first moment indicated the summary of the products of the position of Q and the corresponding intensity, representing the center of the heights of Q_1. The integrated intensity was calculated by the area between the profile and the baseline ($y = 0$ for $S(Q)$ and $y = 1$ for $G(r)$). To analyze the MRO structure, the reduced PDF profile $G(r)$ was transformed to $g(r)$ by $1 + G(r)/4\pi r\rho_0$ (ρ_0 denotes the average number density). The second peak of $g(r)$ characterized the connection mode of the SRO clusters on the MRO scale[50]. The connection modes between the adjacent coordination polyhedrons were divided into four types: 1-atom (vertex sharing), 2-atom (edge sharing), 3-atom (face sharing), and 4-atom (intercross-sharing). To deconvolute the contributions of these connection modes, Gaussian peak fitting was performed on the second coordination shell. First, we calculated the average cluster radius R = 2.969 Å by weighing the bond length of each atom pair of the BAM 11 system[51]. Based on this value, the center distances of the 1-atom, 2-atom, 3-atom, and 4-atom cluster connection modes were determined as 2R, $\sqrt{3}$R, $\sqrt{8/3}$R, and $\sqrt{2}R^3$ respectively. The calculation results of the cluster center distances were input as the initial value for the Gaussian fitting of the second peak of PDF with subtle adjustment (up to ±0.1 Å) to the initial value.

RESULTS AND DISCUSSION

Deformation-induced rejuvenation and shear bands

Figure 1A presents the specific heat capacity curves C_p of the AC, CR- and HPT-deformed BMGs measured at a heating rate of 20 K min^{-1}. The glass transition temperature (T_g), crystallization temperature (T_x), and enthalpy release (ΔH) are summarized in Table 1. Notably, the onset of T_g for the CR- and HPT-deformed BMGs shifted -6 and -7 K, respectively, compared to the AC BMG, suggesting that the glassy states of the deformed BMGs became less stable than those of the AC BMG. Additionally, the relaxation enthalpy before T_g was calculated, indicating that the HPT-deformed BMG exhibited the highest ΔH of 0.656 kJ mol^{-1}. A greater ΔH value implied a more pronounced rejuvenated state in the HPT-deformed BMG[52]. The surface morphology of the CR- and HPT-deformed BMGs (unpolished) was assessed by SEM, revealing a significant proliferation of SBs [Figure 1B and C]. The average spacing between the primary SBs in CR BMG was approximately 7-8 μm [Figure 1B]. By contrast, the HPT BMG exhibited a higher density of shear bands, with an average spacing of about 2 μm [Figure 1C], which was consistent with other reports[41]. Figure 1D-F shows the high-resolution transmission electron microscopy (HRTEM) images of the AC, CR, and HPT BMGs, with insets showing the corresponding selected area electron diffraction (SAED) patterns. As shown

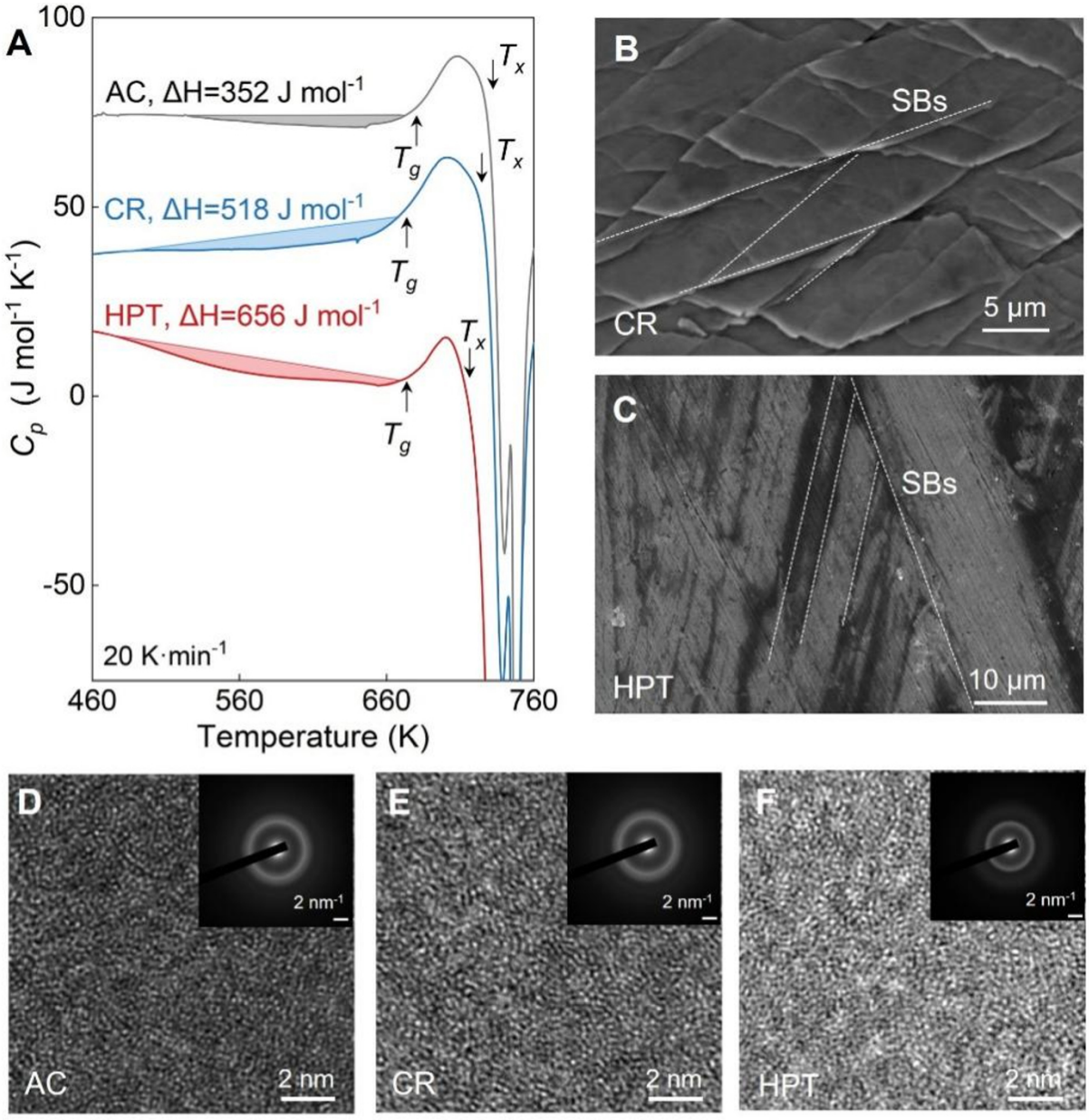

Figure 1. Rejuvenation of BAM 11 metallic glass by pre-plastic deformation. (A) Specific heat capacity C_p curves of AC, CR, and HPT BMGs. The SEM images of the surface of (B) CR and (C) HPT BMGs. Shear bands are marked by white dashed lines. HRTEM images of (D) AC, (E) CR, and (F) HPT BMGs. The insets are SAED patterns.

in Figure 1D, the HRTEM image of the AC-BMG revealed a lower heterogeneity amorphous structure with no discernible crystalline features, which was further confirmed by a diffuse halo in the SAED pattern. By contrast, after deformation processing, the CR [Figure 1E] and HPT [Figure 1F] BMGs exhibited pronounced contrast variations in their HRTEM images while retaining their amorphous nature, as evidenced by the diffuse halos in their respective SAED patterns. The enhancement of structural heterogeneity was most prominent in the HPT sample, where the introduction of extensive shear bands led to more distinct contrast variations in the HRTEM image.

Mechanical softening induced by the shear bands

The nanoindentation results of all BMGs are shown in Figure 2A. The indentation depth under identical loads revealed a clear trend of increasing indentation size with an increasing degree of plastic deformation. For the AC BMG, the hardness and modulus were measured as 6.4 ± 0.1 and 107.8 ± 0.6 GPa, respectively.

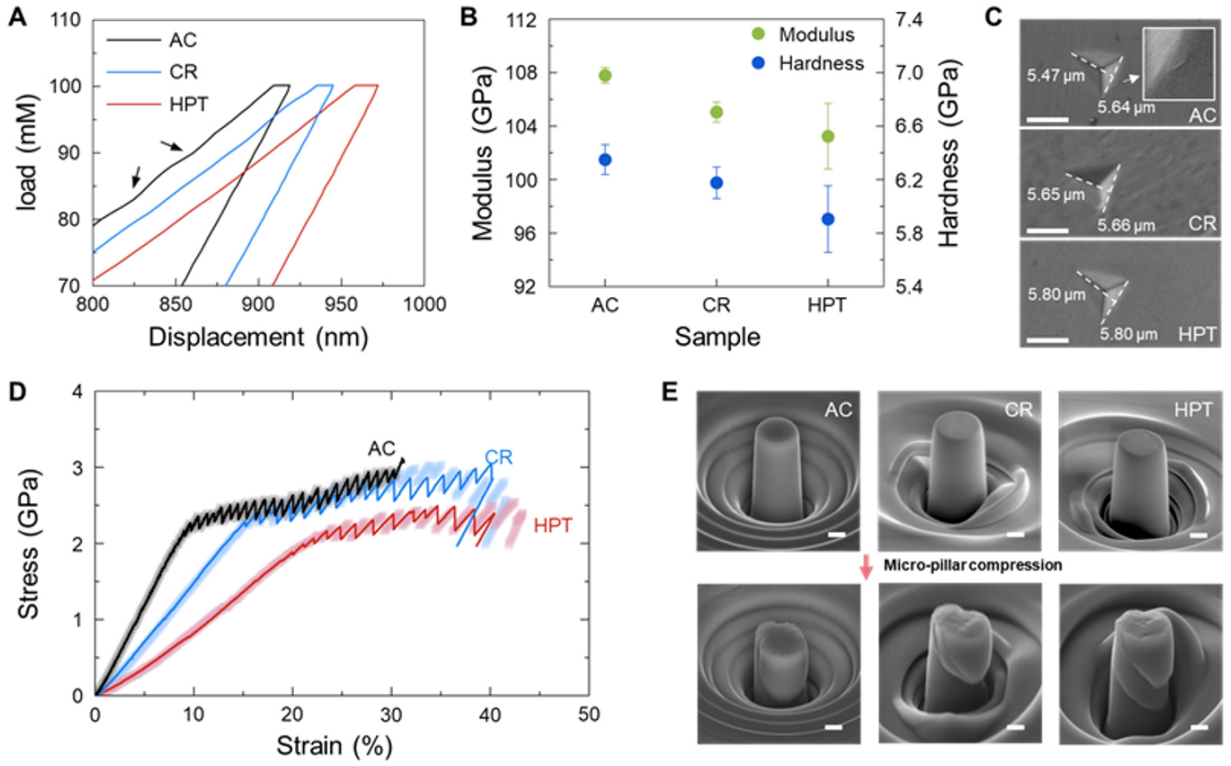

Figure 2. (A) Nanoindentation test results for AC, CR, and HPT BMGs. (B) Hardness and modulus of AC, CR and HPT BMGs from nanoindentation. The error bar indicates the standard deviation through eight tests. (C) The surface morphology of the indentation of AC, CR, and HPT BMGs. The scale bar is 5 μm. (D) The load versus displacement curves of BMG pillars. (E) The morphology of the pillars of AC, CR, and HPT BMGs before and after compression tests. The scale bar is 1 μm.

Table 1. The thermal physical and mechanical parameters of BAM11 BMGs

Sample	T_g (K)	T_x (K)	ΔT_x (K)	ΔH (sub-T_g) (kJ mol^{-1})	Hardness (GPa)
AC	680	731	51	0.352	6.4
CR	674	724	50	0.518	6.2
HPT	673	720	47	0.656	5.9

T_g and T_x is the glass transition and crystallization temperature, respectively, ΔT_x is the width of the supercooled liquid region, ΔH is the enthalpy release below T_g, and the hardness is averaged by eight nanoindentation tests.

For the deformed BMGs, the hardness and modulus were as low as 6.2 ± 0.1 and 105.0 ± 0.8 GPa for the CR BMG and 5.9 ± 0.3 and 103.2 ± 2.5 GPa for the HPT BMG, indicating that both the hardness and modulus decreased with increased spatial heterogeneity [Figure 2B]. Analysis of the indentation depth revealed that under consistent load conditions, the rejuvenated BMGs exhibited larger indentation areas, indicating a macroscopic softening phenomenon in the metallic glass. Furthermore, a small step adjacent to the indentation on the surface of the AC BMG (inset of Figure 2C) was observed, showing shear band propagation. By contrast, the edges of indentation for the CR- and HPT-deformed BMGs were smooth, suggesting that plasticity was improved. A notable feature of the load-displacement response in the AC BMG was the presence of a distinct discontinuous deformation event (black arrows in Figure 2A), typically related to the activation of a single shear band. The discrete event reflected the inhomogeneous plasticity of metallic glass, indicating that discontinuous yielding occurred during plastic deformation. This inhomogeneous deformation was notably absent in both the CR- and HPT-deformed BMGs, suggesting that pre-plastic deformation processing promoted more homogeneous deformation characteristics.

The micropillar compression results, shown in Figure 2D, present the two stress-strain curves (solid and scattered lines) for both the initial and rejuvenated BMGs. This excessive elastic limit beyond the normal level was because the stress-strain curve was not calibrated, highlighting the macro-softening induced by the high volume fraction of SBs. The yield strength of the AC BMG was approximately 2.27 GPa, while the yield strength of the rejuvenated BMGs decreased to 2.25 GPa for CR BMG and 2.11 GPa for HPT BMG. The softening trend was consistent with the hardness trends observed in the nanoindentation tests [Table 1]. Figure 2E reveals the morphologies after compression. The surface of the AC-BMG had only one primary SB, whereas the surface of the rejuvenated BMGs revealed multiple primary SBs accompanied by small secondary shear bands[53]. These findings further confirmed that the introduction of heterogeneous structures (SBs) through pre-deformation improved inhomogeneous plastic deformation.

Structure relaxation behavior of shear bands at sub-T_g temperatures

Figure 3A-C shows the structure factors, $S(Q)$ patterns, of AC, CR, and HPT BMGs at different temperatures. It was evident that the BMGs retained a glassy feature when heated to T_g. Figure 3D-F presents the corresponding differential structure factor, $\Delta S(Q)$ curves, which were obtained by subtracting the $S(Q)$ data at room temperature from that of the corresponding temperature. The variations in $\Delta S(Q)$ curves compared to that of 400 K indicated a sub-T_g structure evolution in the rejuvenated BMGs. As marked by the red dashed line in Figure 3D-F, for the AC BMG, the shape of the $\Delta S(Q)$ patterns developed consistently below T_g. This indicated a typical thermally driven structural change of an amorphous system approaching its glass transition state. However, the $\Delta S(Q)$ curves of the rejuvenated BMGs (CR and HPT) over 400 K exhibited a clear difference from that of the AC BMG. Specifically, they first exhibited a distinct inflection point at lower Q (~2.3 Å^{-1}), reached a maximum, and then followed a similar decreasing trend. This unique shape of the $\Delta S(Q)$ curves in the low-Q region suggested a non-linear, localized ordering process that differed from the uniform evolution observed in the AC BMG.

Further investigations into the *in-situ* heating process were conducted by analyzing the FSDP (Q_1)[54,55]. The first peak position in momentum transfer (first moment of Q_1) was positively correlated with the packing density of the MGs[49,50,56]. As shown in Figure 4A, with an increase in temperature, the first moment of Q_1 for all BMGs initially exhibited an overall decreasing trend due to thermal expansion. The AC BMG exhibited a continuous decrease as the temperature increased to T_g, reflecting a pronounced decrease in packing density. By contrast, the decrease in packing density for the rejuvenated BMGs was suppressed at temperatures far below T_g, implying a competition event in structural evolution that resisted thermal expansion. Due to the introduction of high density of SBs, the atomic mobility was activated in the loosely packed regions, enabling a preferential transition to denser packing during heating. In HPT-BMG, this competition was even more pronounced. This was possibly attributed to the higher volume fraction of SBs in HPT-BMG.

Statistical analysis of the integral intensity of Q_1 was conducted to illustrate the evolution of localized structural ordering in the MGs [Figure 4B]. AC-BMG exhibited a decreasing trend in integral intensity before T_g, followed by an increase after T_g. This evolution in structural ordering has been reported as associated with structural relaxation. The Q_1 integral intensities of all BMGs demonstrated a uniform decreasing trend in the supercooled liquid phase region, followed by a rapid increase after reaching the T_x temperature, signifying the rapid convergence of the structure into an ordered state during crystallization. After heating, the slope of the integrated intensity initially exhibited a decreasing trend. Subsequently, enhanced atomic mobility in the shear-affected zones promoted structural ordering, leading to an opposite shift in both CR BMG and HPT BMG. This trend reversal was more intense in HPT BMG with greater plastic deformation. Also, the temperature at which these two competing mechanisms reached equilibrium was denoted as T_r.

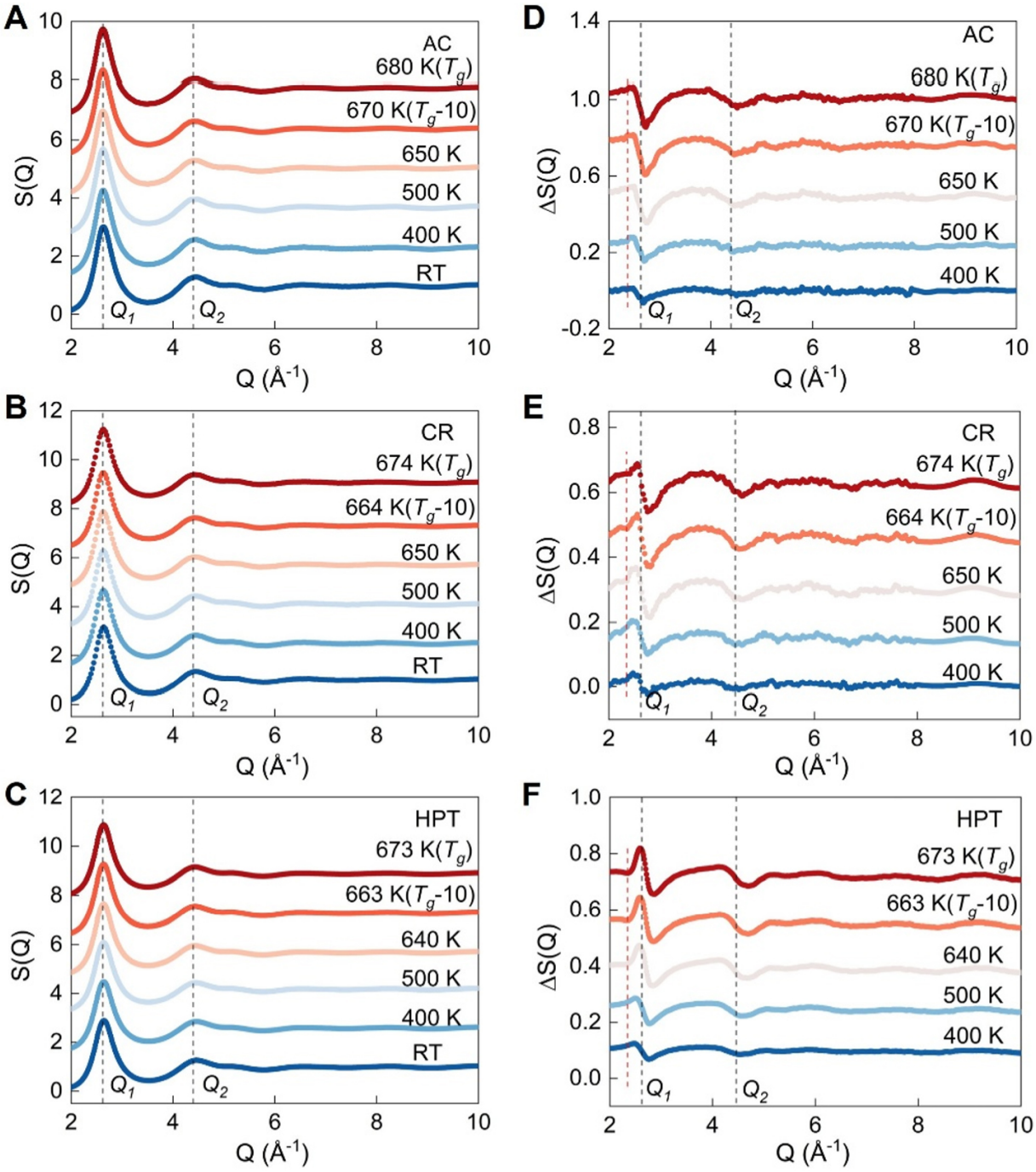

Figure 3. The *in-situ* synchrotron X-ray diffraction patterns at different temperatures of the (A) AC, (B) CR, and (C) HPT BMGs during heating. Difference $\triangle S(Q)$ profiles obtained by subtracting the diffraction pattern at RT for the (D) AC, (E) CR, and (F) HPT BMGs.

Real space structural analysis was employed to elucidate the structural evolution mechanism in the BMGs. Reduced pair-distribution function, $G(r)$, patterns in Figure 5A-C were derived from the Fourier transformation of the $S(Q)$ profiles. As the temperature approached T_x, all samples exhibited peak splitting, indicating the onset of crystallization. Statistical analysis of the integral intensities, corresponding to the range of $G(r) > 0$ of r_1 and r_6, provided specific insights regarding structural evolution. A relative coordinate axis was adopted for comparison, with the Y-axis range set to the average value of each curve ±10%. A notable commonality was that as the temperature increased to T_g, the integral intensities of r_1 and r_6

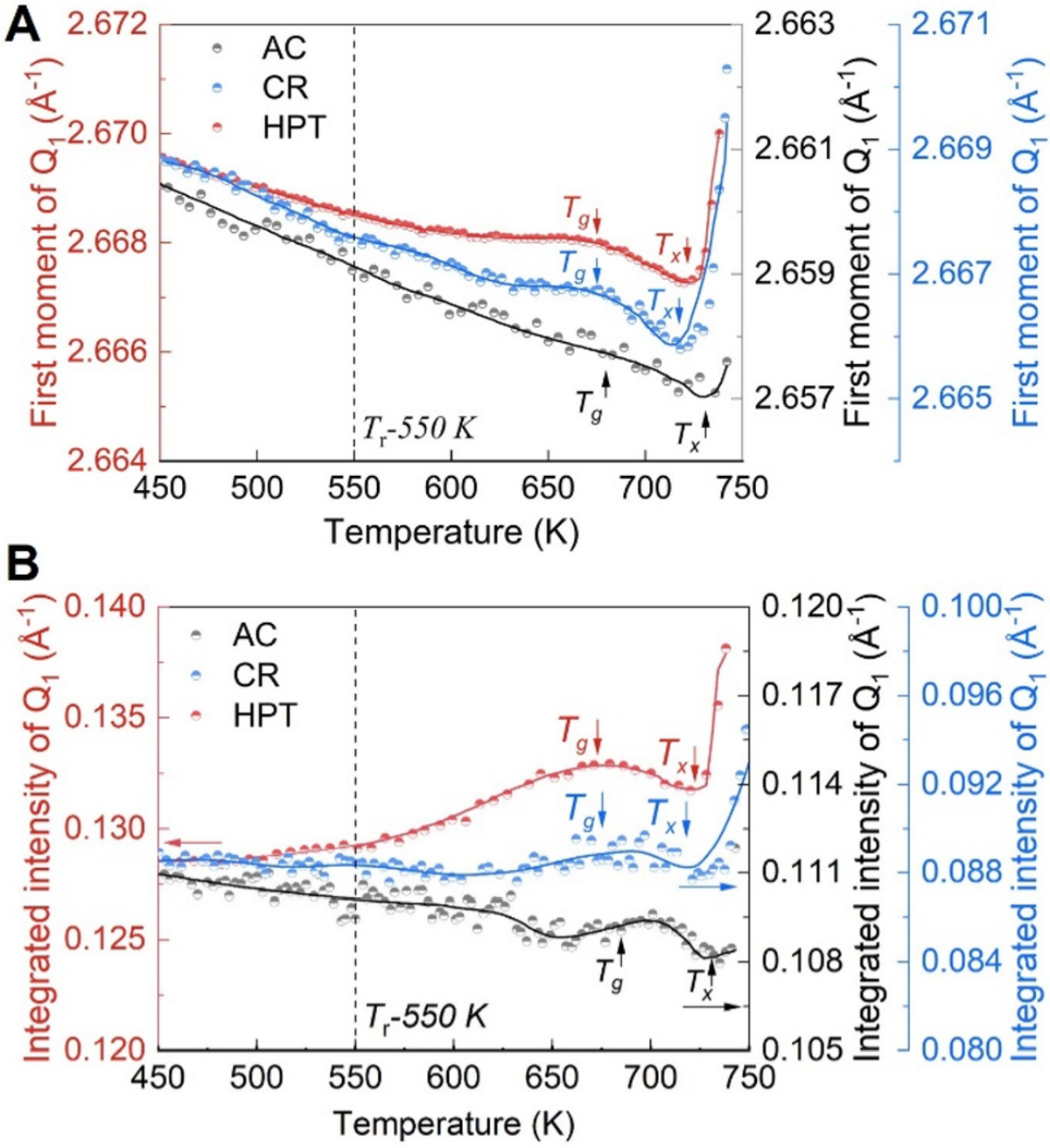

Figure 4. Emergence of medium-range ordering at sub-T_g in different BMGs. (A) First moment and (B) integrated intensity of the first sharp diffraction peak (Q_1) of $S(Q)$ profile of AC, CR and HPT BMGs as a function of temperature. The solid lines are obtained by spline fitting of the raw data. The onset temperature of relaxation (T_r) is marked by the dashed line in the figures.

transitioned from a gradual increase (starting at T_r) to a rapid increase, corresponding to a rapid relaxation process. For AC-BMG, the changes in the intensities of r_1 and r_6 were smaller than those in the rejuvenated BMGs, and the temperature at which rapid relaxation occurred was higher [Figure 5D]. Conversely, CR- and HPT-BMG, which possessed a higher volume fraction of SBs, exhibited a lower T_r, indicating that the introduction of SBs directly modulated atomic mobility, thereby influencing rapid relaxation [Figure 5E]. Although the trends of r_1 and r_6 during relaxation remained consistent in HPT-BMG, it was evident that the changes in the r_6 peak, representing MRO, were more pronounced [Figure 5F]. This indicated that the structural relaxation prior to T_g was primarily driven by contributions from medium-range order. Based on

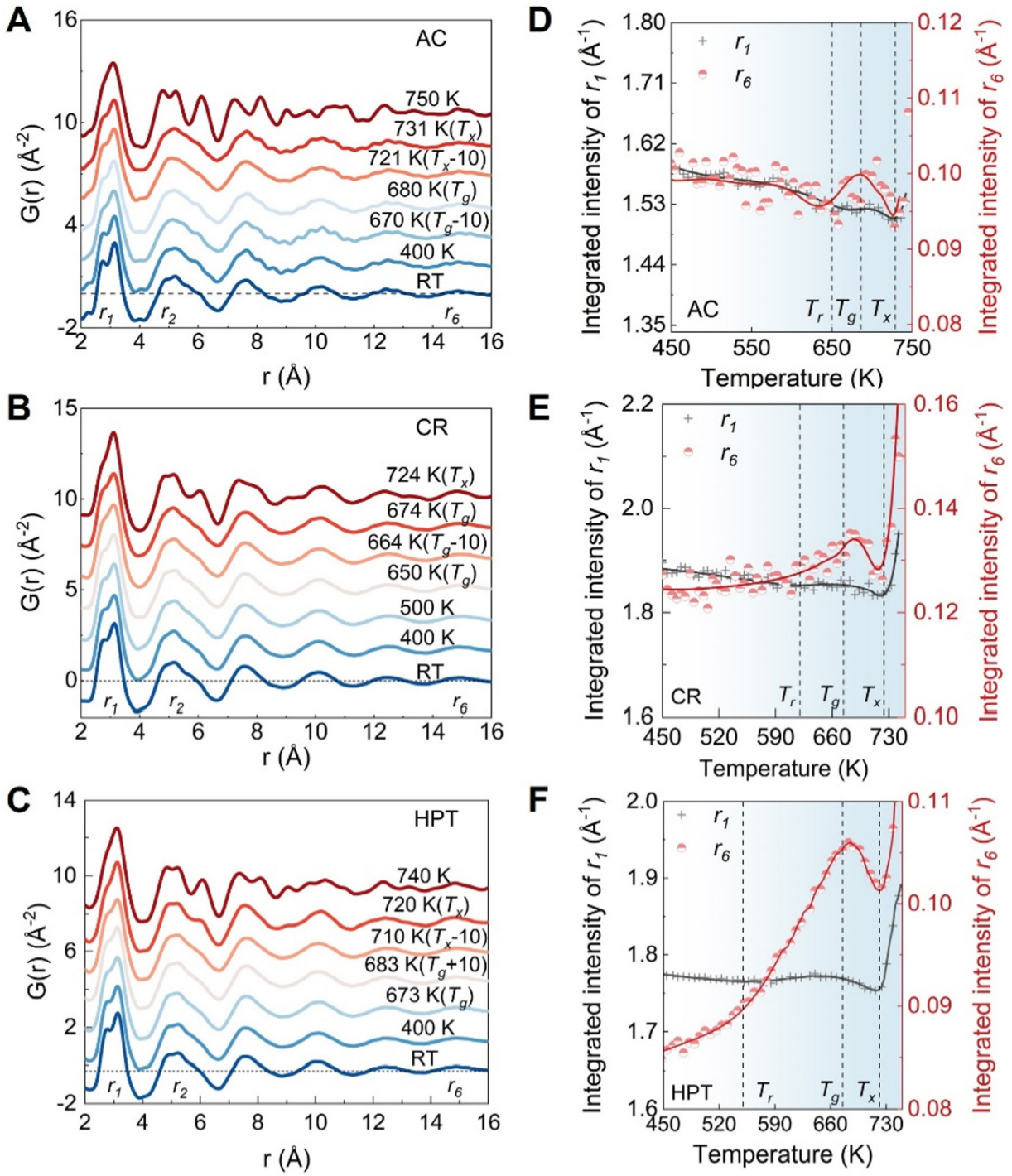

Figure 5. Pair-distribution function, *G*(*r*), of (A) AC, (B) CR, and (C) HPT BMGs during *in-situ* heating process. Integrated intensity of *G*(*r*) over the first (r_1) and sixth (r_6) shell (for regions where $G(r) \geq 0$) for (D) AC, (E) CR, and (F) HPT BMGs.

the above analysis, we concluded that the introduction of SBs through plastic deformation facilitated the rapid activation of MRO during the relaxation process, thereby promoting structural ordering below T_g.

Based on previous studies, the MRO structures could be reflected by correlations among atoms in the second-nearest-neighbor shell and accessed by analyzing the radial distribution of central atoms within local short-range order (SRO) units[57]. Figure 6A demonstrates the connection models between inter-polyhedra,

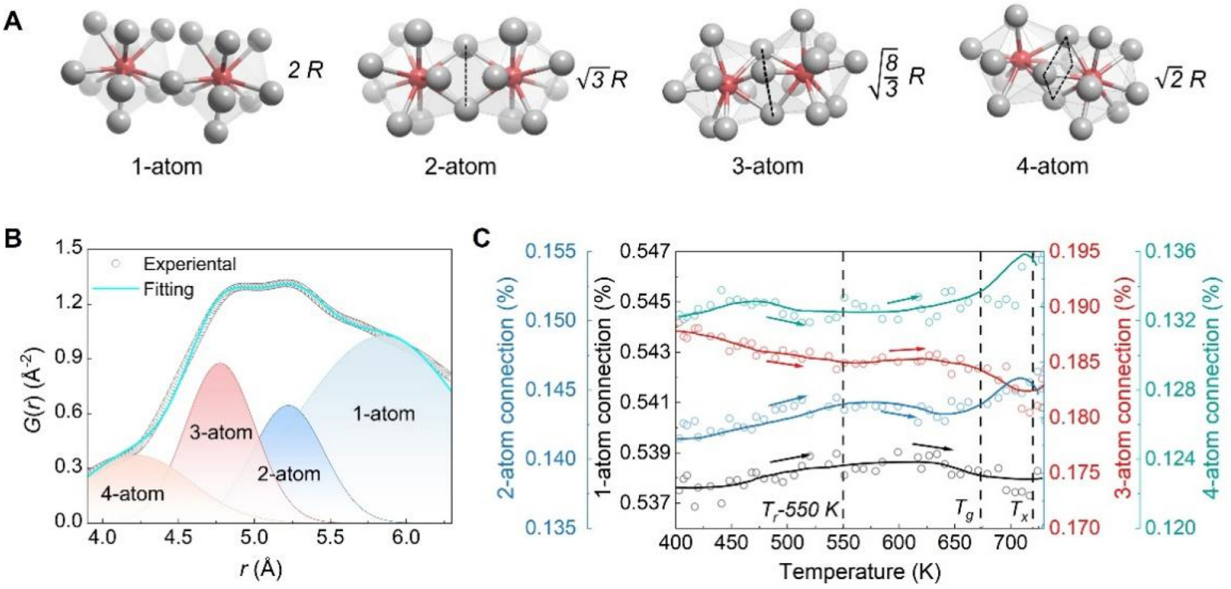

Figure 6. (A) Schemes of the four different cluster connection modes. (B) Gaussian fitting result for the 2nd shell of the *g*(*r*) pattern of HPT BMG at room temperature. (C) The contribution of each connection mode of the HPT BMG during *in situ* heating process.

including 1-atom, 2-atom, 3-atom, and 4-atom sharing configurations, and variations in these connection modes could alter MRO ordering. The cluster center distances for these four connection modes could be calculated geometrically as 2R, $\sqrt{3}$R, $\sqrt{8/3}$R, and $\sqrt{2}$R , where R denotes the average cluster radius (detailed in Materials and Methods). In multi-peak decoupling, the use of Gaussian fitting was justified by the random deviation of atomic positions from their equilibrium distance caused by thermal fluctuations, following normal statistics near the average nearest neighbor distance[58]. Figure 6B illustrates the Gaussian fitting of the second PDF peak for HPT-BMG at room temperature, while Figure 6C demonstrates the proportional evolutions of each connection mode during *in situ* heating process. In the overall heating process, a trade-off relationship was observed between the 1- and 4-atom modes and 2- and 3-atom modes. We found that before T_r, the proportion of 1- and 2-atom patterns tended to increase, while the proportion of 3- and 4-atom patterns decreased. The increased fraction of 1- and 2-atom modes indicated looser packing in MRO dominated by thermal expansion. Within a certain temperature range below T_g, the proportion of 1- and 2-atom modes started to decrease, whereas that of the 3- and 4-atom modes increased. This indicated that the overall structural order of the samples before T_r still decreased under the thermal effect, but the rate of decrease started to slow. After T_r, the structural order improved due to the enhanced relaxation behavior, which was possibly promoted by the emergence of more ordered 3- and 4-atom connection modes where the distance between the SRO clusters was shorter.

CONCLUSIONS

In conclusion, a clear structure engineering-mechanical property correlation was revealed through state-of-the-art characterization techniques and analysis. The introduction of different volume fractions of shear bands into BAM11 BMG by mechanical deformation could alter different rejuvenation states with higher energy states. The rejuvenated BMG exhibited more significant structural relaxation at sub-T_g, which was associated dominantly with enhanced ordering at medium-range scale. Specifically, this MRO ordering process was characterized by a competitive evolution between different cluster connection modes, where the transition from 2-atom to 3-atom connections dominated. Our findings suggested that a high energy state could be obtained through severe plastic deformation, which in turn resulted in significantly enhanced sub-T_g structural ordering behavior at the medium-range scale. Our study offers novel insights into the

atomic structure origins of shear bands and provides a model for the design of Zr-based metallic glasses with high plasticity.

DECLARATIONS

Acknowledgments

The authors thanked the staff of beamline BL13SSW at Shanghai Synchrotron Radiation Facility for the support of synchrotron data analyses. Thanks to Yin Z.X. for the help in sample preparation in the preliminary.

Authors' contributions

Supervised the project: Lan, S.; Zhu, H.
Cast and processed the CR-BMG: Yao, Z.; Ying, H.; Zhang, W.
Cast and processed the HPT-BMG: Yao, Z.; Jiang, Y.; Lin, H.; Edalati, K.
Prepared micro-pillar specimens and performed the micro-pillar compression: Yao, Z.
Prepared the TEM specimens: Yao, Z.; Liu, S.; Ge, J.
Performed *in-situ* synchrotron X-ray diffraction experiments at 11-ID-C of APS, ANL: Lan, S.; Liu, S.; Ren, Y.
Analyzed the PDF results: Zeng, J.; Lan, S.; Wu, Z.; Liu, S.; Ren, Y.; Wang, X. L.
Performed the TEM work: Lan, S.; Yao, Z.; Liu, S.
Drafted the manuscript together: Lan, S.; Wu, Z.; Liu, S.; Yao, Z.
All authors analyzed and reviewed the results and provided input to this paper.

Availability of data and materials

The data that support the findings of this study are available from the corresponding author upon reasonable request.

AI and AI-assisted tools statement

Not applicable.

Financial support and sponsorship

This work was financially supported by the National Natural Science Foundation of China (Grant Nos. 12261160364, 52573263, 52222104, 22275089, and 52571196), funded by Basic Research Program of Jiangsu (Grant No. BK20253026), the Natural Science Foundation of Jiangsu Province (Grant No. BK20200019), the Fundamental Research Funds for the Central Universities (No. 30922010307), the Research Grants Council of the Hong Kong Special Administrative Region, Project N_CityU173/22, and the support by Guangdong-Hong Kong-Macao Joint Laboratory for Neutron Scattering Science. Wu, Z. acknowledges the financial support by Guangdong Talent Program (no. 2024TQ08C536). This research used the Advanced Photon Source, a US Department of Energy (DOE) Office of Science User Facility operated for the DOE Office of Science by Argonne National Laboratory under Contract No. DE-AC02–06CH11357, and was supported by the US DOE Office of Science, Office of Basic Energy Sciences.

Conflicts of interest

Ren, Y. is a Senior Editorial Board Member of the journal *Microstructures*. Lan, S. is an Editorial Board Member of the journal *Microstructures*. Ren, Y. and Lan, S. were not involved in any steps of editorial processing, notably including reviewers' selection, manuscript handling and decision making, while the other authors have declared that they have no conflicts of interest.

Ethical approval and consent to participate

Not applicable.

Consent for publication

Not applicable.

REFERENCES

1. Ma, E.; Ding, J. Tailoring structural inhomogeneities in metallic glasses to enable tensile ductility at room temperature. *Mater. Today.* **2016**, *19*, 568-79. DOI
2. Greer, A. L. Metallic glasses. *Science* **1995**, *267*, 1947-53. DOI PubMed
3. Liu, Z.; Yang, Y.; Liu, C. Yielding and shear banding of metallic glasses. *Acta. Mater.* **2013**, *61*, 5928-36. DOI
4. Yazdani, A.; Dewitt, D.; Huang, W.; et al. Mechanical properties of an ultrahard in situ amorphous steel matrix composite. *Adv. Eng. Mater.* **2024**, *26*, 2400257. DOI
5. Di, S.; Wang, Q.; Zhou, J.; et al. Enhancement of plasticity for FeCoBSiNb bulk metallic glass with superhigh strength through cryogenic thermal cycling. *Scr. Mater.* **2020**, *187*, 13-8. DOI
6. Qiao, J.; Wang, Y.; Pelletier, J.; Keer, L. M.; Fine, M. E.; Yao, Y. Characteristics of stress relaxation kinetics of $La_{60}Ni_{15}Al_{25}$ bulk metallic glass. *Acta. Mater.* **2015**, *98*, 43-50. DOI
7. Xu, N.; Huang, Y.; Cao, Y.; Li, S.; Wang, Y. D. Novel casting CoCrNiAl eutectic high entropy alloys with high strength and good ductility. *Microstructures* **2023**, *3*, 2023015. DOI
8. Argon, A. Plastic deformation in metallic glasses. *Acta. Metall.* **1979**, *27*, 47-58. DOI
9. Wang, Q.; Lou, H.; Xu, D.; et al. Shear straining promoted structural transition in bulk metallic glasses. *Scr. Mater.* **2024**, *249*, 116168. DOI
10. Greer, A.; Cheng, Y.; Ma, E. Shear bands in metallic glasses. *Mater. Sci. Eng. R. Rep.* **2013**, *74*, 71-132. DOI
11. Ketov, S. V.; Sun, Y. H.; Nachum, S.; et al. Rejuvenation of metallic glasses by non-affine thermal strain. *Nature* **2015**, *524*, 200-3. DOI
12. Wu, G.; Liu, S.; Wang, Q.; et al. Substantially enhanced homogeneous plastic flow in hierarchically nanodomained amorphous alloys. *Nat. Commun.* **2023**, *14*, 3670. DOI PubMed PMC
13. Wright, W.; Saha, R.; Nix, W. Deformation mechanisms of the $Zr_{40}Ti_{14}Ni_{10}Cu_{12}Be_{24}$ bulk metallic glass. *Mater. Trans.* **2001**, *42*, 642-9. DOI
14. Wang, W. H. The elastic properties, elastic models and elastic perspectives of metallic glasses. *Prog. Mater. Sci.* **2012**, *57*, 487-656. DOI
15. Turnbull, D. Under what conditions can a glass be formed? *Contemp. Phys.* **1969**, *10*, 473-88. DOI
16. Huang, R.; Suo, Z.; Prevost, J.; Nix, W. Inhomogeneous deformation in metallic glasses. *J. Mech. Phys. Solids.* **2002**, *50*, 1011-27. DOI
17. Falk, M. L.; Langer, J. S. Dynamics of viscoplastic deformation in amorphous solids. *Phys. Rev. E.* **1998**, *57*, 7192-205. DOI
18. Schuh, C.; Hufnagel, T.; Ramamurty, U. Mechanical behavior of amorphous alloys. *Acta. Mater.* **2007**, *55*, 4067-109. DOI
19. Sun, W.; Li, T.; Wang, Y.; et al. Thermally-driven structural inhomogeneity and serrated plastic flow in TaTiZr amorphous medium-entropy alloy. *Acta. Mater.* **2025**, *286*, 120764. DOI
20. Wang, W. H. Dynamic relaxations and relaxation-property relationships in metallic glasses. *Prog. Mater. Sci.* **2019**, *106*, 100561. DOI
21. Tao, K.; Qiao, J.; He, Q.; Song, K.; Yang, Y. Revealing the structural heterogeneity of metallic glass: mechanical spectroscopy and nanoindentation experiments. *Int. J. Mech. Sci.* **2021**, *201*, 106469. DOI
22. Wang, Z.; Sun, B. A.; Bai, H. Y.; Wang, W. H. Evolution of hidden localized flow during glass-to-liquid transition in metallic glass. *Nat. Commun.* **2014**, *5*, 5823. DOI PubMed
23. Ma, E. Controlling plastic instability. *Nat. Mater.* **2003**, *2*, 7-8. DOI PubMed
24. Lv, J.; Yin, D.; Wang, F.; Yang, Y.; Ma, M.; Zhang, X. Influence of sub-Tg annealing on microstructure and crystallization behavior of TiZr-based bulk metallic glass. *J. Non. Cryst. Solids.* **2021**, *565*, 120855. DOI
25. Song, K.; Pauly, S.; Sun, B.; et al. Formation of Cu-Zr-Al-Er bulk metallic glass composites with enhanced deformability. *Intermetallics* **2012**, *30*, 132-8. DOI
26. He, L.; Wu, S.; Dong, A.; et al. Selective laser melting of dense and crack-free $AlCoCrFeNi_{2.1}$ eutectic high entropy alloy: synergizing strength and ductility. *J. Mater. Sci. Technol.* **2022**, *117*, 133-45. DOI
27. Hadibeik, S.; Ghasemi-Tabasi, H.; Burn, A.; Lani, S.; Spieckermann, F.; Eckert, J. Controlling the glassy state toward structural and mechanical enhancement: additive manufacturing of bulk metallic glass using advanced laser beam shaping technology. *Adv. Funct. Mater.* **2023**, *34*, 2311118. DOI
28. Argon, A.; Kuo, H. Plastic flow in a disordered bubble raft (an analog of a metallic glass). *Mater. Sci. Eng.* **1979**, *39*, 101-9. DOI
29. Long, Z.; Tao, P.; Wang, G.; et al. Effect of Nb and Ta addition on mechanical properties of Zr-based bulk metallic glasses and composites. *J. Alloys. Compd.* **2022**, *912*, 165071. DOI
30. Kong, L.; Tao, P.; Xiong, Z.; Yan, X.; Yang, Y. Effect of deep cryogenic cycle treatment on the microstructure and mechanical properties of $Zr_{46}Cu_{46}Al_4Ti_4$ bulk metallic glass. *Intermetallics* **2024**, *175*, 108504. DOI

31. Wang, W. H. Correlation between relaxations and plastic deformation, and elastic model of flow in metallic glasses and glass-forming liquids. *J. Appl. Phys.* **2011**, *110*, 053521. DOI
32. Yu, H. B.; Shen, X.; Wang, Z.; Gu, L.; Wang, W. H.; Bai, H. Y. Tensile plasticity in metallic glasses with pronounced *β* relaxations. *Phys. Rev. Lett.* **2012**, *108*, 015504. DOI
33. Greer, A. L.; Sun, Y. H. Stored energy in metallic glasses due to strains within the elastic limit. *Philos. Mag.* **2016**, *96*, 1643-63. DOI
34. Li, X.; Wang, J.; Ke, H.; Yang, C.; Wang, W. Extreme rejuvenation and superior stability in a metallic glass. *Mater. Today. Phys.* **2022**, *27*, 100782. DOI
35. Yuan, X.; Şopu, D.; Spieckermann, F.; et al. Maximizing the degree of rejuvenation in metallic glasses. *Scr. Mater.* **2022**, *212*, 114575. DOI
36. Lee, M.; Lee, K.; Das, J.; Thomas, J.; Kühn, U.; Eckert, J. Improved plasticity of bulk metallic glasses upon cold rolling. *Scr. Mater.* **2010**, *62*, 678-81. DOI
37. Scudino, S.; Jerliu, B.; Surreddi, K.; Kühn, U.; Eckert, J. Effect of cold rolling on compressive and tensile mechanical properties of $Zr_{52.5}Ti_5Cu_{18}Ni_{14.5}Al_{10}$ bulk metallic glass. *J. Alloys. Compd.* **2011**, *509*, S128-30. DOI
38. Stolpe, M.; Kruzic, J.; Busch, R. Evolution of shear bands, free volume and hardness during cold rolling of a Zr-based bulk metallic glass. *Acta. Mater.* **2014**, *64*, 231-40. DOI
39. Pan, J.; Ivanov, Y. P.; Zhou, W. H.; Li, Y.; Greer, A. L. Strain-hardening and suppression of shear-banding in rejuvenated bulk metallic glass. *Nature* **2020**, *578*, 559-62. DOI PubMed
40. Dmowski, W.; Yokoyama, Y.; Chuang, A.; et al. Structural rejuvenation in a bulk metallic glass induced by severe plastic deformation. *Acta. Mater.* **2010**, *58*, 429-38. DOI
41. Gunderov, D.; Churakova, A.; Boltynjuk, E.; et al. Observation of shear bands in the Vitreloy metallic glass subjected to HPT processing. *J. Alloys. Compd.* **2019**, *800*, 58-63. DOI
42. Nieh, T.; Yang, Y.; Lu, J.; Liu, C. Effect of surface modifications on shear banding and plasticity in metallic glasses: an overview. *Prog. Nat. Sci. Mater. Int.* **2012**, *22*, 355-63. DOI
43. Chen, W.; Chan, K.; Chen, S.; Guo, S.; Li, W.; Wang, G. Plasticity enhancement of a Zr-based bulk metallic glass by an electroplated Cu/Ni bilayered coating. *Mater. Sci. Eng. A.* **2012**, *552*, 199-203. DOI
44. Qu, R.; Wu, S.; Wang, S.; Wang, X.; Zhang, Z. Shear banding stability and fracture of metallic glass: effect of external confinement. *J. Mechan. Phys. Solids.* **2020**, *138*, 103922. DOI
45. Ding, J.; Patinet, S.; Falk, M. L.; Cheng, Y.; Ma, E. Soft spots and their structural signature in a metallic glass. *Proc. Natl. Acad. Sci. USA.* **2014**, *111*, 14052-6. DOI PubMed PMC
46. Hubek, R.; Seleznev, M.; Binkowski, I.; Peterlechner, M.; Divinski, S. V.; Wilde, G. The impact of micro-alloying on relaxation dynamics in Pd40Ni40P20 bulk metallic glass. *J. Appl. Phys.* **2018**, *124*, 225103. DOI
47. Zhou, H.; Hubek, R.; Peterlechner, M.; Wilde, G. Two-stage rejuvenation and the correlation between rejuvenation behavior and the boson heat capacity peak of a bulk metallic glass. *Acta. Mater.* **2019**, *179*, 308-16. DOI
48. Ebner, C.; Escher, B.; Gammer, C.; Eckert, J.; Pauly, S.; Rentenberger, C. Structural and mechanical characterization of heterogeneities in a CuZr-based bulk metallic glass processed by high pressure torsion. *Acta. Mater.* **2018**, *160*, 147-57. DOI
49. Qiu, X.; Thompson, J. W.; Billinge, S. J. L. *PDFgetX2*: a GUI-driven program to obtain the pair distribution function from X-ray powder diffraction data. *J. Appl. Crystallogr.* **2004**, *37*, 678. DOI
50. Lan, S.; Blodgett, M.; Kelton, K. F.; Ma, J. L.; Fan, J.; Wang, X. Structural crossover in a supercooled metallic liquid and the link to a liquid-to-liquid phase transition. *Appl. Phys. Lett.* **2016**, *108*, 211907. DOI
51. Ding, J.; Ma, E.; Asta, M.; Ritchie, R. O. Second-nearest-neighbor correlations from connection of atomic packing motifs in metallic glasses and liquids. *Sci. Rep.* **2015**, *5*, 17429. DOI PubMed PMC
52. Révész, Á.; Arjmandabasi, T.; Schafler, E.; Browne, D. J.; Kovács, Z. Comprehensive thermal analysis of a high stability Cu-Zr-Al bulk metallic glass subjected to high-pressure torsion. *J. Therm. Anal. Calorim.* **2023**, *148*, 2323-34. DOI
53. Louzguine-Luzgin, D.; Ketov, S.; Wang, Z.; Miyama, M.; Tsarkov, A.; Churyumov, A. Plastic deformation studies of Zr-based bulk metallic glassy samples with a low aspect ratio. *Mater. Sci. Eng. A.* **2014**, *616*, 288-96. DOI
54. Ren, Z. Q.; Churakova, A.; Wang, X.; et al. Enhanced tensile strength and ductility of bulk metallic glasses $Zr_{52.5}Cu_{17.9}Al_{10}Ni_{14.6}Ti_5$ via high-pressure torsion. *Mater. Sci. Eng. A.* **2021**, *803*, 140485. DOI
55. Ma, D.; Stoica, A. D.; Wang, X. Power-law scaling and fractal nature of medium-range order in metallic glasses. *Nat. Mater.* **2008**, *8*, 30-4. DOI PubMed
56. Li, F.; Wang, T.; He, Q.; et al. Micromechanical mechanism of yielding in dual nano-phase metallic glass. *Scr. Mater.* **2018**, *154*, 186-91. DOI
57. Yao, Z.; Zhu, H.; Lou, Y.; et al. Composition engineering of short-range-ordered polyhedra in Ni-Mo-P-B metallic glass for electrochemical sensing. *Mater. Today.* **2026**, *94*, 103245. DOI

58. Knuyt, G.; De Schepper, L.; Stals, L. M. Calculation of some metallic glass properties, based on the use of a Gaussian distribution for the nearest-neighbour distance. *Philos. Mag. B.* **2006**, *61*, 965-88. DOI